Cerium and gallium containing mesoporous bioactive glass nanoparticles for bone regeneration: Bioactivity, biocompatibility and antibacterial activity

Fatih Kurtuldu [a,b], Nurshen Mutlu [a,b], Martin Michálek [a], Kai Zheng [b], Milan Masar [c], Liliana Liverani [b], Si Chen [a], Dušan Galusek [a,d,*], Aldo R. Boccaccini [b,**]

[a] FunGlass, Alexander Dubček University of Trenčín, 911 50 Trenčín, Slovakia
[b] Institute of Biomaterials, Department of Material Science and Engineering, University of Erlangen-Nuremberg, 91058 Erlangen, Germany
[c] Centre of Polymer Systems, University Institute, Tomas Bata University in Zlin, 760 01 Zlin, Czech Republic
[d] Joint Glass Centre of the IIC SAS, TnU AD and FChFT STU, Centre for Functional and Surface Functionalized Glass, TnU AD, Trenčín, Slovakia

ABSTRACT

In recent years, mesoporous bioactive glass nanoparticles (MBGNPs) have generated great attention in biomedical applications. In this study, cerium and gallium doped MBGNPs were prepared by microemulsion assisted sol-gel method in the binary SiO_2-CaO system. MBGNPs with spheroidal and pineal shaped morphology were obtained. Nitrogen sorption analysis elucidated the mesoporous structure of synthesized nanoparticles with high specific surface area. X-ray diffraction analysis confirmed the amorphous nature of the nanoparticles. The chemical compositions of all samples were determined by inductively coupled plasma-optical emission spectrometry (ICP-OES), which revealed that the contents of cerium and gallium could be tailored by adjusting the concentrations of the precursors used for the synthesis. All MBGNPs exhibited in vitro bioactivity when immersed in simulated body fluid, except the particles doped with higher amounts than 1 mol% of cerium. MBGNPs showed antibacterial activity against *S. aureus* and *E. coli* without exhibiting cytotoxicity towards MG-63 osteoblast-like cells. Mentioned features of the obtained Ce and Ga-doped MBGNPs make them useful for multifunctional applications such as drug delivery carriers or bioactive fillers for bone tissue engineering applications.

1. Introduction

Bioactive glasses (BGs) are being increasingly considered in a variety of biomedical applications including in mesoporous particulate form [1–5]. Mesoporous silica nanoparticles were discovered in 1992 [6], while Vallet-Regi et al. proposed mesoporous silica as a drug delivery system in 2001 [7]. Mesoporous silica nanoparticles (MSNs) offer a higher specific surface area and tunable pore structure (such as pore size and pore volume) compared with traditional sol-gel derived BGs [8]. Therefore, MSNs exhibit interaction with tissues at the cellular level and directly with the extracellular matrix [9–12]. Although such MSNs are of great interest, they have not yet been approved by regulatory agencies for biomedical applications. Especially there is a concern that MSNs could remain in the body for an extended period of time [13]. However, the dissolution behavior of MSNs can be altered by the addition of modifier cations into the silica network. Soluble and easily biodegradable BGs have been considered for clinical applications for over 30 years with Na, Ca, and P being the elements added to silica in standard (45S5) BG [14]. In this sense, the addition of cations like Ca^{2+} can alter MSNs degradation rate, affecting the fate of MNPs in the body [13]. Instead mesoporous bioactive glass nanoparticles (MBGNPs) have been developed. The addition of metallic ions affects the surface charges of silica nanoparticles, which can result in their aggregation, disturbing their growth [15].

The microemulsion-assisted sol-gel method is often used to synthesize MBGNPs [15–18]. The size of the resulting particles is defined by the size of the oil droplets which serve as nanoreactors. Structure directing agents like cetyltrimethylammonium bromide (CTAB) are used to form mesopores [19]. CTAB is a well known cationic surfactant regularly used to form mesoporous structures through the formation of

micelles under basic conditions [15,20]. It has been also reported that CTAB could alter the shape of the particles from spherical to rod-like [20]. If hydrophobic ethyl acetate (EA) molecules are added into the solution of water and CTAB, the CTAB micelles self-assemble with EA to form oil in water (O/W) microemulsion droplets [16]. The surfactants stabilize the microemulsion drops and the oil phases may act as barriers that prevent the nanoparticles from aggregating [15,21]. Particles with good dispersity and homogenous compositions can be produced and additional metal ions can be included using this approach [16,17,22,23]. However, the addition of metal ions was reported to affect the concentration of calcium in MBGNPs significantly [17].

Therapeutic inorganic ions are added to BGs considering their specific functions in the body (e.g. osteogenesis and angiogenesis, antibacterial activity, immunomodulator, and potential effects in cancer treatment). The obtained BGs-doped with those biologically active ions can be used as multifunctional platforms for several applications [17,22,23]. In fact, along with therapeutic ions, mesoporous nanoparticles can release also other agents (e.g., enzymes, drugs, or growth factors) from their mesopores to stimulate tissue regeneration [24]. Recently, zinc-doped mesoporous silica nanoparticles were developed for cancer therapy [25]. Zinc has potential as an anticancer agent in the form of zinc oxide, which gives promising results against breast cancer cells [25]. There are various examples showing the suitability of MBGNPs for the delivery of antitumor drugs or imaging agents to cancer cells [26]. Chen et al. [25] reported the direct delivery of therapeutic cations' to treat diseases like cancer, as a very recent approach to use therapeutic ions in cancer treatment. Therapeutic ions are also used for their reported antibacterial activity, which is needed to develop antibiotic-free antibacterial materials [27]. For example, Paterson et al. developed copper-doped MBGNPs which showed inhibition effect against Gram-positive and Gram-negative bacteria with a broad range of antibacterial activity for healing chronic wounds [28].

Cerium is another therapeutic ion receiving increasing attention in biomedical applications [18,29]. There is evidence showing that cerium favors osteoblast growth, improves mechanical properties of bone, stimulates bone formation, and exhibits antibacterial properties [30–33]. Cerium possesses multi-enzyme mimetic properties. It can mimic enzymes like superoxide dismutase, catalase, and oxidase, which confers biological effects, such as antioxidant properties [34]. Additionally, cerium can change its oxidation states (Ce^{4+} and Ce^{3+}) in physiological fluids, reducing reactive oxygen species (ROS) [18]. The reduction of excessive ROS is essential to retain healthy biological functions [18,33]. Cerium doped mesoporous bioactive glasses (MBGs) have been synthesized by a sol-gel based method [32]. Varini et al. [34] used cerium containing MBG as bioactive filler in alginate beads to increase their bioactivity and pro-osteogenic activity. Zheng et al. [18] incorporated Ce into MBGNPs by a two-step approach via post-modification method: the prepared nanoparticles exhibited anti-inflammatory response and pro-osteogenic activity. However, to the best of our knowledge, the direct addition of cerium into MBGNPs during the sol-gel synthesis has not been reported so far. In addition, this study sheds light on the effect of the direct addition of cerium on particles' morphology, glass composition, and cell response.

Gallium ions have been also reported to promote osteogenesis and to exhibit antibacterial activity [27]. Ga^{3+} ions share certain similarities with Fe^{3+}. Thus Gallium can bond with iron-binding proteins instead of Fe, inhibiting their biological function [35]. Ga ions were found to be beneficial in treating localized infections, inhibiting biofilm formation, and imparting bactericidal activity against free-living bacteria and biofilm cells [36]. Ga^{3+} has been proposed for the treatment of bone resorption, autoimmune diseases, for inhibition of biofilm formation, and for bone, colon, and prostate cancer treatments [27]. Gallium-containing mesoporous bioactive glasses (MBGs) synthesized mainly by evaporation induced self-assembly (EISA) method have been studied previously [32,37]. However, to the best of our knowledge, the synthesis of Ga-doped MBGNPs is novel. These cerium and gallium nanoparticles

Table 1
Theoretical compositions of mesoporous bioactive glass nanoparticles (mol%).

MBGNPs type	SiO$_2$	CaO	Ce$_2$O$_3$	Ga$_2$O$_3$
40CaS	60	40	–	–
30CaS	70	30	–	–
20CaS	80	20	–	–
Ce1	60	39	1	–
Ce3	60	37	3	–
Ce5	60	35	5	–
Ga1	60	39	–	1
Ga3	60	37	–	3
Ga5	60	35	–	5

are thus of great interest for applications as bioactive fillers and drug delivery platforms.

In the present study, we synthesized for the first time cerium and gallium doped MBGNPs in the binary SiO$_2$-CaO system via a microemulsion assisted sol-gel method. The influence of the addition of CaO (between 20 and 40 mol%) on the physicochemical properties of MBGNPs and the addition of cerium and gallium (up to 5 mol%) was studied. The base composition for the addition of cerium and gallium was selected taking into consideration the physicochemical properties of calcium-containing MBGNPS. Metallic precursors were added directly during the sol-gel process. Undoped and the novel Ce and Ga doped MBGNPs were extensively characterized in terms of morphology, microstructure, composition, apatite formation ability, dissolution behavior, antibacterial properties, and cytotoxicity with osteoblast-like cells.

2. Materials and methods

2.1. Materials

Tetraethyl orthosilicate (TEOS, 100%, 24,004.290 VWR International), hexadecyltrimethylammonium bromide (CTAB, BioXtra, ≥99%, H9151, Sigma-Aldrich), calcium nitrate tetrahydrate, Ca(NO$_3$)$_2$ • 4H$_2$O, 99.1%, VWRVN261, VWR), ethyl acetate (99.7%, L-00028, Centralchem), ammonium hydroxide (ACS reagent, 28.0–30.0% NH$_3$ basis, 221,228, Sigma-Aldrich), cerium nitrate hexahydrate (CN, 99.95%, 238,538, Treibacher) and gallium nitrate hexahydrate (99.999%, 480,854, Alchemica) were used. All chemicals were of analytical grade.

2.2. Synthesis of mesoporous bioactive glass nanoparticles

MBGNPs were synthesized by microemulsion assisted sol-gel method as previously reported in the literature [16]. Three series of processes were set out, including a calcium (undoped) series (20, 30 and 40 mol %), a cerium doping series denoted as 60SiO$_2$-(40-x)CaO-xCe$_2$O$_3$, and a gallium doping series denoted as 60SiO$_2$-(40-x)CaO-xGa$_2$O$_3$, where x = 1, 3 and 5 mol%. The samples with different compositions were respectively denoted as 40CaS, 30CaS, 20CaS, Ce1, Ce3, Ce5, Ga1, Ga3, and Ga5. Table 1 shows the theoretical compositions of all synthesized MBGNPs. The fabrication procedure of MBGNPs can be briefly described as follows: 2.8 g of CTAB was dissolved in 150 mL deionized water under continuous stirring for 30 min at 30 °C. Then 40 mL of ethyl acetate and 3.66 mL of ammonium hydroxide were added and the solution was left stirring for 30 min. 14.4 mL of TEOS and appropriate amounts of calcium nitrate tetrahydrate, cerium nitrate hexahydrate, or gallium nitrate hexahydrate were added stepwise in 30 min intervals. After stirring for 4 h, the precipitates were separated by centrifugation and washed 2 times with deionized water and 1 time with ethanol. Collected particles were dried at 60 °C overnight before the calcination step. Finally, the dried samples were calcinated by heating the dried articles at 1 °C/min to 650 °C with 3 h dwell time.

2.3. Materials characterization

The morphology and qualitative compositional analyses were performed using scanning electron microscopy (SEM, JEOL 7600F, and Zeiss Auriga Base) equipped with an energy dispersive spectroscopy (EDS) instrument (Bruker, Oxford Instruments). Samples were dispersed in ethanol and dropped on an aluminum substrate and dried in air. The average particle size (diameter) was determined by ImageJ software (National Institutes of Health, Bethesda, MD, USA): at least 100 particles were measured for each sample. XRD was performed using X-ray powder diffractometer MiniFlex 600 with Cu Kα radiation in the 2Θ range of 20° – 60°. A step size of 0.020° and dwell time of 1 s per step were used. Samples were dispersed on a low background silicon wafer (Bruker, AXS) before measurement. Fourier transform infrared spectroscopy (FTIR, IRAffinity-1S spectrophotometer, SHIMADZU, Japan) was carried out in transmission mode in the wavenumber range from 4000 to 400 cm^{-1}, scan speed of 40 scans/min, and at a resolution of 4 cm^{-1}. To determine the chemical compositions of MBGNPs quantitatively, 25 mg of each sample was used for the chemical analysis by ICP-OES (Agilent 5100, SVDV). The closed vessel microwave-assisted digestion (Speedwave 4, Berghof Products+ Instruments, Germany) was applied using a digestion solution prepared from 6 mL of HCl (35%), 2 mL of HNO$_3$ (69%), and 0.5 mL of HF (48%) to dissolve the MBGNPs for the analysis. To prevent the formation of poorly soluble fluorides in the presence of alkali earth elements [36] and to avoid corrosion of silica parts of the instrument by HF, 5 mL of H$_3$BO$_3$ was added to the acid mixture. The solutions of digested samples were diluted using ultrapure water to 50 mL before measurement. The multielement solution was prepared by adding Sc (10 mg/L) and Be (1 mg/L) as internal standards. Since silica forms volatile complexes (like H$_2$SiF$_6$) in the presence of HF, its exact amount could not be determined from the measurement and was calculated by adding to 100%. The N$_2$ adsorption-desorption method was used to determine the surface area and pore size distribution using Bellsorp mini II gas adsorption analyzer (Microtrac, Japan) with isotherm at 77 K. The surface area was obtained by the Brunauer-Emmet-Teller (BET) method. The pore size was determined by the Barrett-Joyner-Halenda (BJH) method.

2.4. In vitro bioactivity

The ability of MBGNPs to form hydroxyapatite (HA) was tested by in vitro bioactivity tests [38]. 75 mg of MBGNPs were immersed in 50 mL of simulated body fluid (SBF), prepared according to Kokubo's method [39], at 37 °C with an agitation speed of 120 rpm for 1, 3, 7, and 14 days. After immersion, samples were collected and washed with deionized water and acetone, and characterized by SEM and FTIR.

2.5. Ion release in PBS

The ion release test was performed in phosphate buffer saline (PBS). 75 mg of MBGNPs were immersed in 50 mL of PBS at 37 °C with an agitation of 120 rpm for 1, 3, 7, and 14 days. After immersion, all samples were filtered using a 0.22 μm pore size filter for removing nanoparticles. All filtrates were analyzed using ICP-OES (Agilent 5100 SVDV). A series of three calibration solutions was prepared to obtain the working curve from the certified reference materials for Si^{2+}, Ca^{2+}, Ce^{3+}, and Ga^{3+} (Analytica, Prague, Czech Republic), which were diluted to prepare the stock calibration solutions. The internal standardization technique with scandium was used to eliminate the non-spectral interferences. The precision of the analysis for all ions was below 5%. Each sample was analyzed in triplicate.

2.6. Antibacterial assay

S. aureus (Gram-positive) and *E. coli* (Gram-negative) bacteria were used to evaluate the antibacterial activity of MBGNPs. Both bacteria were cultivated in lysogeny broth (LB) medium (Luria/Miller) at 37 °C for 24 h. MBGNPs were sterilized at 160 °C for 3 h in a furnace (Naberthem, Germany). After sterilization, 1% *w/v* of MBGNPs were added in LB medium and incubated at 37 °C for 24 h. Afterward, the suspensions were filtered using a 0.22 μm pore size filter to obtain particle-free supernatant.

Optical density (OD) of the bacteria suspension was detected at 600 nm using a visible light spectrophotometer (Thermo Scientific GENESYS 30, Germany) and it was set up at 0.015, which corresponds to 20 μL of bacterial suspension and equals ≈1.10^7 colony forming units (CFU)/mL. 10% w/v of each MBGNPs extract were added into bacteria suspensions and incubated at 37 °C for 3, 6, and 24 h, and LB medium and bacteria suspensions were used as a control group. OD values at 600 nm were measured at each time point. The relative viability of the bacteria was calculated as follows:

$$Relative\ bacteria\ viability\ (\%) = \frac{OD_{Sample}}{OD_{Control}} \times 100$$

2.7. In vitro cytotoxicity assay

The cytocompatibility evaluation was carried out using a human osteoblast-like cell line from the European Collection of Authenticated Cell Cultures (MG-63, ECACCS, Sigma Aldrich, Darmstadt, Germany). The MG-63 cell line is a human osteoblast-like cell line that has been used as a model in bone research for many years. These cells exhibit the functional characteristics of a pre-osteoblastic stage and have been successfully applied for studying cell-material interactions, including cell adhesion and proliferation on biomaterials [17]. Due to these reasons, the MG-63 cell line was selected for the study. The MG-63 cells were maintained in cell culture medium (Dulbecco's Modified Eagle Medium, DMEM, Gibco, Germany) containing 10 vol% fetal bovine serum (FBS, Sigma-Aldrich, Germany) and 1 vol% penicillin/streptomycin (Gibco, Germany) at 37 °C in a humidified atmosphere of 95% air and 5% CO$_2$.

MG-63 cells were seeded into 24-well plates with an inoculum ratio of 1×10^5 cells/mL and incubated at 37 °C in a humidified atmosphere of 5% CO$_2$ for 24 h. MBGNPs samples were sterilized by heat treatment at 160 °C for 3 h in a furnace (Naberthem, Germany). Then 1 g of sterilized MBGNPs was added in 10 mL of DMEM (10% *w/v*) and incubated under the same condition as the cells (24 h in the atmosphere with 5% CO$_2$). Afterwards, the extracts were collected by centrifugation and filtering using a 0.22 μm pore size filter to eliminate any solid residues. The extracts were diluted to 1, 0.1 and 0.01% w/v using DMEM. All the extracts of 10, 1, 0.1, and 0.01% w/v were placed in contact with MG-63 cells in 24-well plates and incubated for 48 h. Cells cultured in the medium were used as positive control and cells in DMEM with 6 vol% dimethyl sulfoxide (DMSO) were used as a negative control. Each sample was prepared in triplicate.

Cell viability was detected using WST-8 assay (CCK-8 Kit, Sigma-Aldrich, Germany). 400 μL of 1% *v/v* WST-8 in a colourless cell medium solution was added in each well and incubated for 3 h. Pure WST-8 solution was also incubated and used as blank. Aliquots of 100 μL from each well were transferred to a 96 well-plate for spectrometry measurements with a microplate reader (PHOmo, Anthos Mikrosysteme GmbH, Germany) at 450 nm. The experiments were performed in triplicate. The cell viability was calculated as follow:

$$Cell\ viability\ (\%) = \frac{(Absorbance\ of\ sample - Absorbance\ of\ blank)}{(Absorbance\ of\ positive\ control - Absorbance\ of\ blank)} \times 100$$

2.8. Cell morphology

MG-63 cells were stained using Hematoxylin & Eosin (H&E). Hematoxylin binds to the DNA/RNA and stains them dark blue or violet. Eosin binds to the amino acids/protein including cytoplasmic filaments
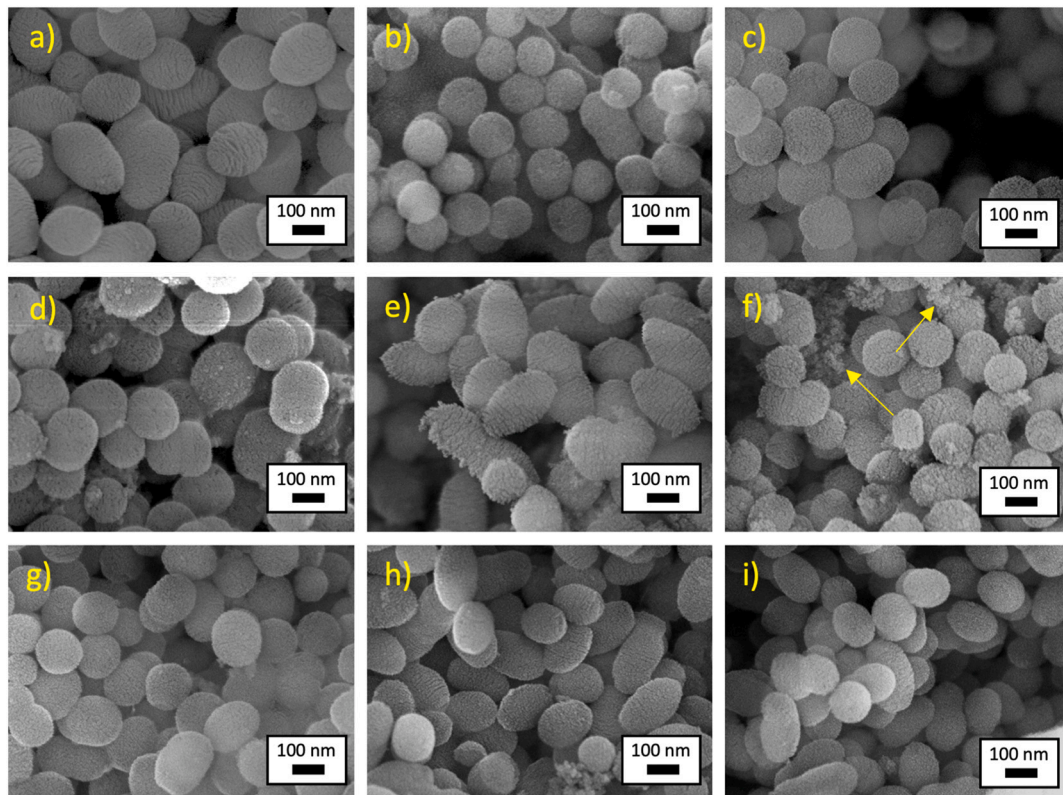
Fig. 1. SEM micrographs showing the morphology of MBGNPs. a) 40CaS, b) 30CaS, c) 20CaS, d) Ce1, e) Ce3, f) Ce5, g) Ga1, h) Ga3 and i) Ga5.

Table 2
Textural properties and particle size of MBGNPs. S_{BET}: Surface area, V_P: Total pore volume, D_P: Average pore diameter (Total pore volume at $p/p_0 = 0.990$).

MBGNPs type	S_{BET} (m^2/g)	V_P (cm^3/g)	D_P (nm)	Particle size (nm)
40CaS	345	0.43	4.9	195 $\pm$ 32
30CaS	546	0.46	3.4	153 $\pm$ 35
20CaS	677	0.86	5.1	171 $\pm$ 21
Ce1	412	0.69	6.7	174 $\pm$ 22
Ce3	343	0.77	8.9	189 $\pm$ 56
Ce5	314	0.73	9.3	130 $\pm$ 24
Ga1	486	0.61	5.1	174 $\pm$ 39
Ga3	401	0.61	6.1	156 $\pm$ 35
Ga5	469	0.64	5.4	146 $\pm$ 25

and intracellular membranes and stains them red/pink. After discarding the WST solution from the 24 well-plates, the cells were washed with PBS, and fixed using 4% solution of paraformaldehyde in PBS, and washed with deionized water, then stained with hematoxylin for 10 min. Afterwards, the samples were washed with tap water and Scott's tap water and then washed with deionized water for 5 min. Samples were then stained using eosin solution (0.1% *w/v* Eosin, 60% v/v EtOH, 5% v/v acetic acid and 35% v/v ultra-pure water) for 5 min, washed with 95% and 99.5% ethanol, and dried at room temperature. The morphology of cells was observed using an optical microscope (Primo vert, Carl Zeiss).
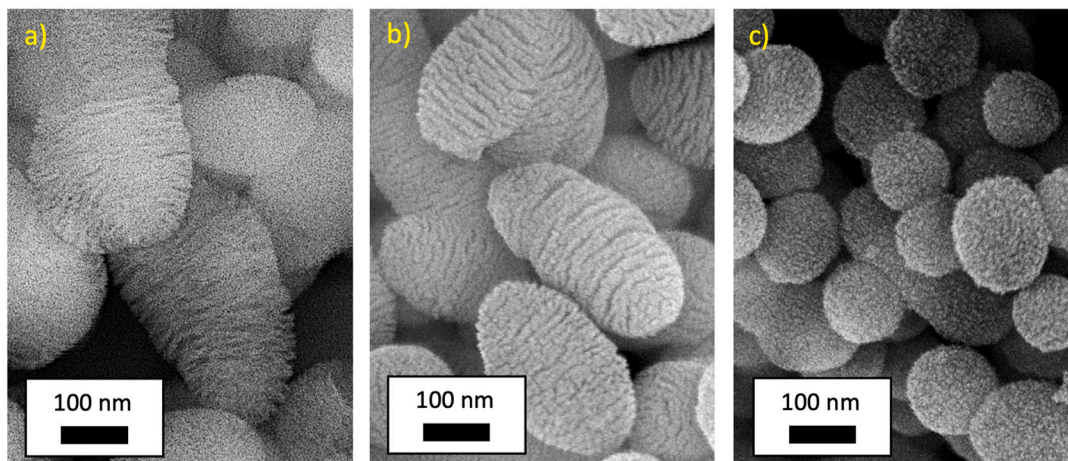

Fig. 2. SEM micrographs of different pore and surface structures of MBGNPs, a) and b) pineal shaped nanoparticles from 40CaS, and c) spherical shaped nanoparticles from 30CaS.
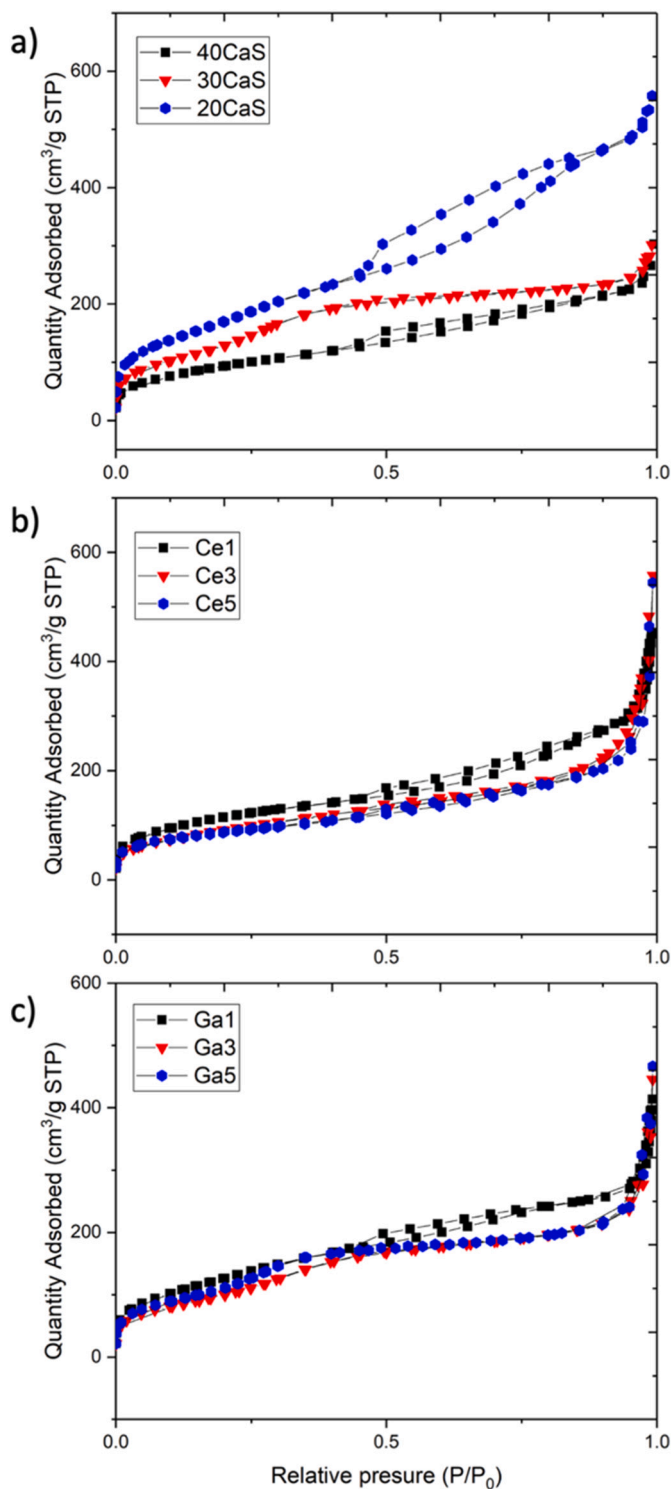
Fig. 3. Nitrogen adsorption–desorption isotherm plots of MBGNPs: a) XCaS series, b) CeX series and c) GaX series compositions.

2.9. Statistical analysis

Statistical analysis was performed by one-way ANOVA and Bonferroni's test using software Origin 2017 (OriginLab, Northampton, MA, USA). Probability (P) values $P < 0.05$ were considered to represent statistically significant differences. The results were expressed as mean ± standard deviation (SD).

Table 3

Actual compositions of MBGNPs (mol%) measured by ICP-OES.

MBGNPs type	SiO$_2$	CaO	Ce$_2$O$_3$	Ga$_2$O$_3$
40CaS	86.7 ± 0.4	13.3 ± 0.4	–	–
30CaS	90.3 ± 0.5	9.7 ± 0.5	–	–
20CaS	92.1 ± 0.5	7.9 ± 0.5	–	–
Ce1	88.5 ± 0.2	10.1 ± 0.2	1.4 ± 0.1	–
Ce3	88.7 ± 0.5	6.6 ± 0.3	4.7 ± 0.2	–
Ce5	92.6 ± 0.8	1.0 ± 0.1	6.5 ± 0.7	–
Ga1	90 ± 2	9 ± 1	–	0.9 ± 0.2
Ga3	88.3 ± 0.3	8.7 ± 0.2	–	3.0 ± 0.3
Ga5	89.4 ± 0.3	5.3 ± 0.2	–	5.4 ± 0.2

3. Results and discussions

3.1. Morphological and structural characterization of MBGNPs

SEM micrographs of MBGNPs are shown in Fig. 1. The micro-emulsion assisted sol-gel method allowed the preparation of MBGNPs with a spherical shape, homogeneous size distribution, and a low degree of agglomeration. Different amounts of calcium nitrate affected the morphology of the samples. The shape of MBGNPs changed from elongated pineal to spherical with the decrease of the amount of calcium nitrate. These morphological changes can be related to the metallic ions interactions with the N atom of the CTAB molecule via ionic bonds [15,40]. The size of the MBGNPs ranged within the interval of 136 ± 25 nm (Table 2). Fig. 2 shows more detailed surface structures of spherical and pineal-shaped MBGNPs with the compositions 40CaS and 30CaS. According to SEM analysis pineal shaped MBGNPs have lamellar pore structure while spherical-shaped MBGNPs have radial pore structure: these results are in agreement with data from literature [16].

In both cases, nitrogen adsorption-desorption isotherms of 40CaS and 30CaS showed type IV isotherm patterns. The H3-type and H4-type hysteresis loops were observed for 40CaS and 30 CaS samples, respectively (Fig. 3). This indicated slit-shaped pores in 40CaS and narrow slit pores in 30CaS [41]. Table 2 summarizes the values of specific surface area, total pore volume, and average pore diameter. The increase of the calcium nitrate concentration resulted in lower pore volume and specific surface area. The pore size and structure were not completely homogeneous due to interactions between the cationic Ca^{2+} ions and the cationic surfactant CTAB during the reaction. This interaction negatively affects the self-assembly of micelles to form mesophases [15].

Table 3 shows the actual composition of MBGNPs. The molar percentages of oxides were calculated from the results of ICP-OES: all elements were considered in oxide form. According to the ICP-OES results, the 40CaS composition contains the highest amount of CaO. Literature also shows that additional doping elements usually result in decreasing amount of calcium in similar systems [17,42]. For these reasons, 40CaS was selected as the basic composition for cerium and gallium addition.

Cerium-doped MBGNPs exhibited spherical or elongated pineal shape, however, the pineal-shaped nanoparticles are more present in Ce3 composition, as seen in Fig. 1e. Apart from the MBGNPs in Ce5, precipitation of irregularly shaped nanoparticles approx. 10 nm in size was observed by SEM (indicated by arrows in Fig. 1f). The irregular nanoparticles are formed by direct precipitation from the cerium nitrate hexahydrate in the presence of a basic environment, e.g. aqueous ammonia [43,44]. The presence of nanoceria is undesirable, especially for drug delivery applications. However, there is a great interest in the applications of cerium oxide as bioactive filler [43]. For example, Matter et al. [45] synthesized cerium oxide nanocrystals and bioactive glass hybrid nanoparticles by spray pyrolysis for possible application as antioxidant, antimicrobial, and biomineralization materials.

All Ce-doped MBGNPs showed type IV isotherm patterns with H3-type hysteresis loop. Ce1 composition showed a higher specific surface area and total pore volume than 40CaS. However, the increase of the doping amount of cerium resulted in decreased specific surface area. On
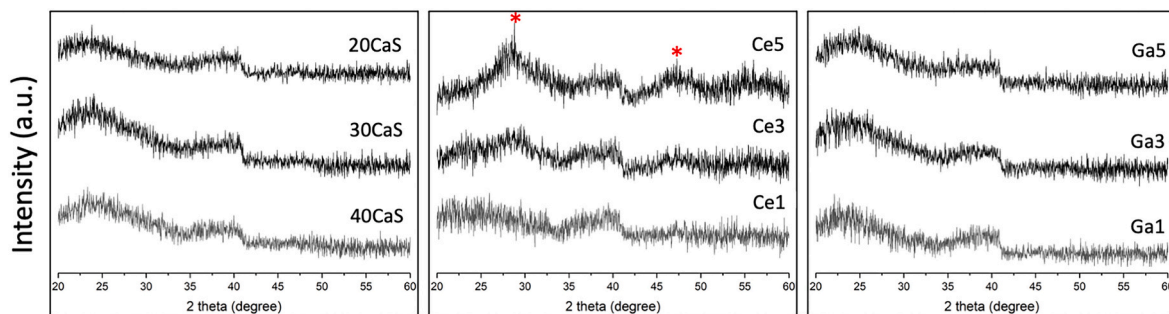
Fig. 4. X-ray diffraction (XRD) patterns of MBGNPs. (* CeO$_2$ (JCPDS number 89–8436)).
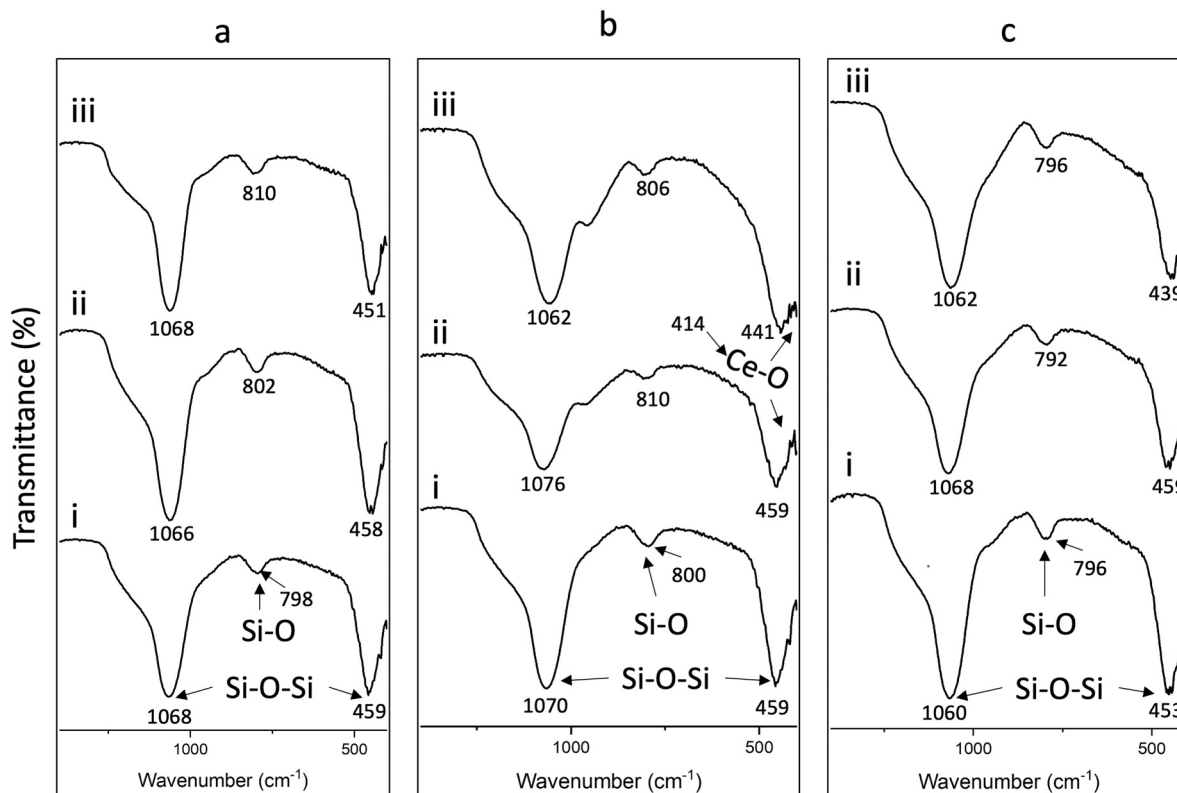

Fig. 5. Fourier-transform infrared (FTIR) spectra between 400 and 1400 cm^{-1} wavenumber of MBGNPs: a) i; 40CaS, ii; 30CaS iii; 20CaS. b) i; Ce1, ii; Ce3 iii; Ce5. c) i; Ga1, ii; Ga3 iii; Ga5 (The relevant peaks are discussed in the text).

the other hand, the total pore volume remained similar, but the pore size increased, reducing the specific surface area.

Table 3 shows the theoretical and actual contents of Ce as a comparison. The content of Ca decreased significantly with the increase of Ce doping concentration. It is noteworthy that nanoceria could not be removed during the centrifugation and washing steps. The presence of nanoceria, therefore, causes the measured content of Ce to be higher than its actual content inside the MBGNPs.

Ga-doped MBGNPs showed both spherical and elongated pineal shapes. In the Ga1 composition spherical shapes were more dominant, while Ga3 and Ga5 compositions showed both spherical and pineal shaped morphologies. Pineal nanoparticles could form by the fusion of microemulsion droplets during the synthesis. In comparison to the Ce doped MBGNPs, the addition of Ga did not result in the formation of gallium oxide nanocrystals. All Ga doped MBGNPs exhibited higher specific surface area than the base 40CaS composition. Their total pore volume and pore diameter also increased compared to 40CaS. The increase of Ga did not affect the total pore volume and pore diameter

significantly. Additionally, the actual amount of gallium doping in MBGNPs was almost identical to the theoretical compositions.

XRD patterns are shown in Fig. 4. The diffraction patterns of all MBGNPs were similar, containing broad bands, which indicated the amorphous nature of the prepared nanoparticles. The only exception was the diffraction pattern of Ce5, which featured discrete diffraction maxima attributed to the face-centered cubic CeO$_2$ phase (JCPDS number 89–8436) [46], confirming that the amount of formed nanoceria was above the detection limit of XRD. Nevertheless, discrete diffraction patterns and the high calcination temperature (650 °C) indicate that Ce^{3+} oxidizes to Ce^{4+}, and CeO$_2$ is a stable phase in the system [44,47].

Fig. 5 shows the FTIR spectra of all prepared samples. A wide band at 1000–1250 cm^{-1} was attributed to the transverse optical mode 1 (TO1) of the Si–O–Si stretching vibration at 1090 cm^{-1} and a TO2 mode of the Si–O–Si stretching vibration at 1220 cm^{-1} [48]. The peak at around 800 cm^{-1} was identified as the Si—O wagging vibration [48]. A peak near 460 cm^{-1} was attributed to the Si–O–Si rocking mode [49]. The absorbance peak at 440 cm^{-1} was ascribed to Ce—O bonds, which belong to
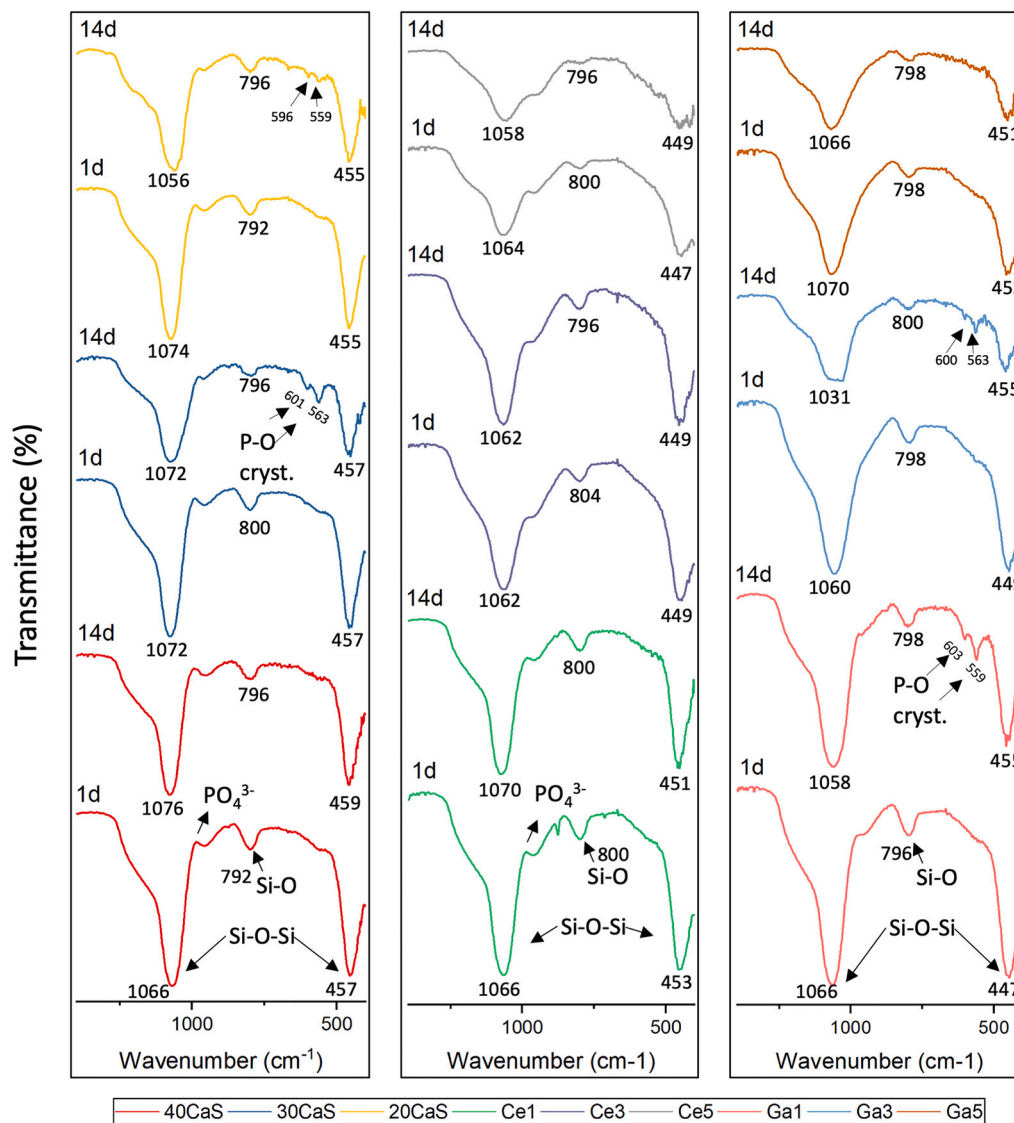
Fig. 6. FTIR spectra between 400 and 1400 cm^{-1} wavenumber of MBGNPs after immersion in SBF for 1 and 14 days (The relevant peaks are discussed in the text).

crystalline cerium oxide active phonon modes in a range of 800–400 cm^{-1} [47,50].

3.2. In-vitro bioactivity

Fig. 6 shows the FTIR spectra of all MBGNPs after immersion in SBF at 37 °C for 1 day and 14 days. Except for Ce3 and Ce5 compositions, all particles showed in vitro bioactivity demonstrated by the presence of a band between 900 and 1000 cm^{-1} associated with the stretching modes of the PO$_4^{3-}$ bonds in HA, which was identified after 1-day immersion in SBF. The band in the region of 600 cm^{-1} corresponds to amorphous phosphate [51].

SEM micrographs of MBGNPs after immersion in SBF for 7 days are shown in Fig. 7. HA crystals can be observed on the surface of all samples, and the Ca/P ratio on the MBGNPs surface was calculated by the contents of Ca and P obtained through EDS. The Ca/P ratio on the MBGNPs surface was close to 1.64 which is similar to the Ca/P ratio in HA [52]. Needle-like crystals of HA could be observed on the surface of 30CaS. The crystals of HA on 40CaS and 20CaS compositions possessed cauliflower-like morphology, which has been commonly found when bioactive glasses are immersed in SBF [38]. Fig. 8 shows high magnification SEM micrographs of different types of crystal structures on 40CaS

and 30CaS samples. The extent of HA crystal formation, as reported in SEM micrographs, was the highest for Ce1 composition after 7 days. Due to the lower content of Ca, Ce3, and Ce5 compositions showed similar results only after 14 days of immersion. All Ga-doped MBGNPs showed the formation of a similar type of HA crystals on the surface. Increasing the amount of gallium doping resulted in significant refinement of precipitated HA crystals (Fig. 7; g, h, i). Different sizes and morphology of HA crystals could be attributed to different compositions and surface topographies of MBGNPs. However, since the calcium content could not be fixed for all compositions, it is difficult to differentiate the influence of individual parameters on the size of HA crystals. The highest calcium content was measured in Ga1: the concentration of Ca in the solution will therefore achieve the limit of supersaturation with respect to HA earlier. The HA nucleation then starts sooner, and the HA crystals have more time and higher Ca concentration to grow than in other compositions.

3.3. Ion release test in PBS

The ion release profiles of MBGNPs immersed in PBS are shown in Fig. 9. The ion release profile of the material gives information about its degradation, kinetics, bioactive response, antibacterial properties, and
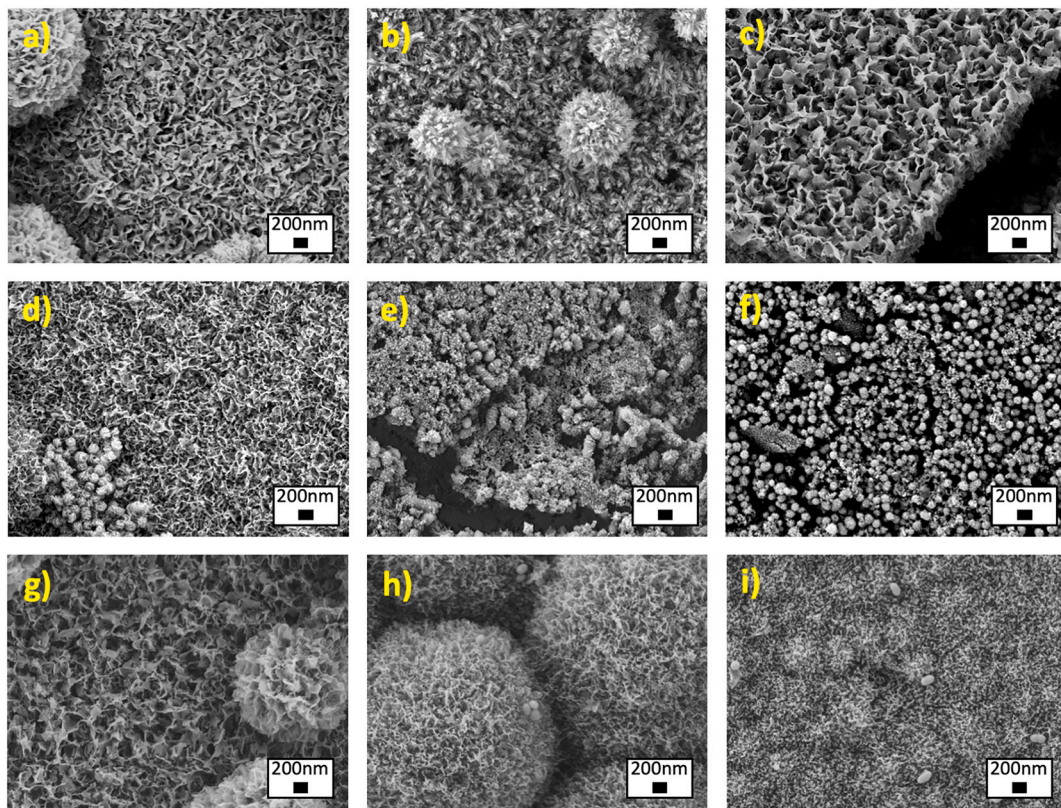
Fig. 7. SEM micrographs of MBGNPs after 7 days of immersion in SBF. a) 40CaS, b) 30CaS, c) 20CaS, d) Ce1, e) Ce3, f) Ce5, g) Ga1, h) Ga3 and i) Ga5.
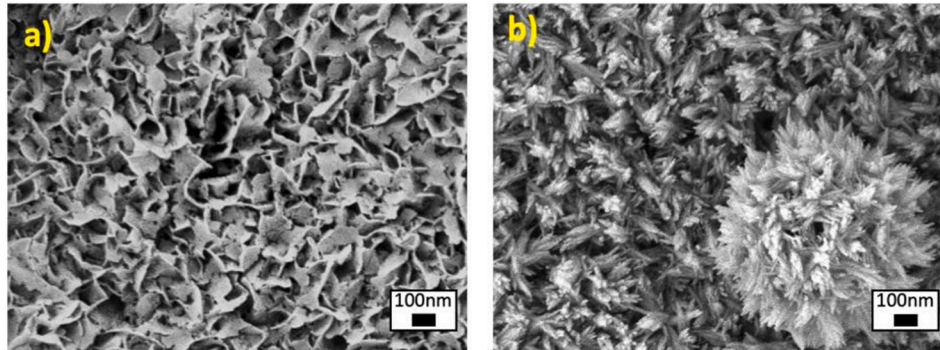

Fig. 8. SEM micrographs of a) 40CaS, b) 30CaS compositions after 7 days in SBF.

cytotoxicity. In order to be bioactive, a glass should be partially soluble and the concentration of Ca^{2+}, PO_4^{3+}, and Si^{4+} ions in the medium should increase at the beginning of immersion. Later, the content of Ca and P in the medium decreases if a calcium phosphate layer is formed, indicating in vitro bioactivity. The MBGNPs synthesized in this work do not contain phosphorus. However, as shown by Martinez et al. [51], binary CaO-SiO$_2$ glass produced by the sol-gel method could form an apatite layer by taking phosphorus from the medium, such as SBF.

For the xCaS series of MBGNPs, all release profiles of Si were similar. There was a burst release after one day of immersion. The concentrations of released Si increased with increasing Ca content, with the highest release of Si measured for 40CaS composition. Calcium is a network modifier and it decreases the network connectivity: because of that, the increase of Ca content in synthesized MBGNPs caused higher solubility of the nanoparticles. On the other hand, 40CaS showed the lowest concentration of Ca compared with the 30CaS and 20CaS samples, which is a contradiction with the actual Ca content in 40CaS. This

difference could be attributed to the fact that the actual amount of Ca released in the initial period of immersion is so high that the supersaturation of the solution occurs with respect to the formation of HA. A HA layer is then formed earlier than in 30CaS and 20CaS compositions, binding the released Ca ions. As a consequence, the measured concentration of Ca in the solution is quite low. For other compositions, the trend of increased Ca concentrations after 1 day of immersion, and the later decrease, is similar.

All Ce-doped MBGNPs showed identical Si release profiles. After 7 days of immersion, the Si concentrations gradually stabilized at around 60 mg/L for all Ce-doped MBGNPs. For all Ce-doped samples, a burst release of Ca was observed during the 1st day of immersion. Ce1 composition showed a high release of Ca. In fact, Ce1 has the highest specific surface area (412 m^2/g) and the highest content of CaO (10.1 $\pm$ 0.2 mol%), which explains the different release profiles. The Ce5 composition showed the lowest concentration of Ca compared to other samples. This result could be explained by the actual compositions, with
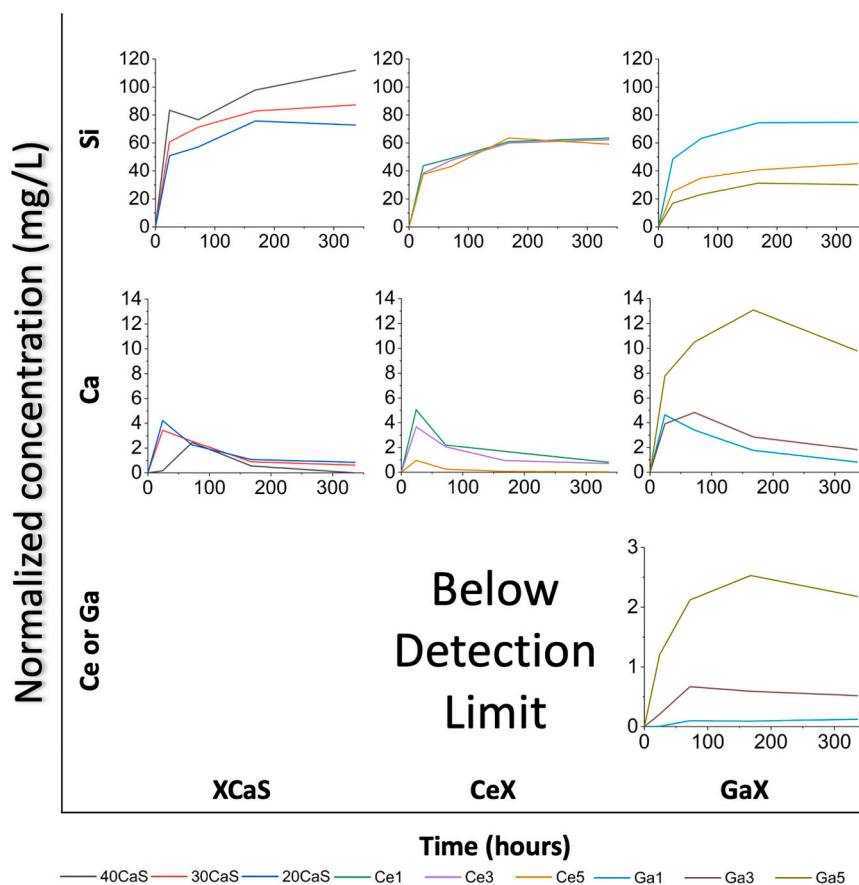
Fig. 9. – Ion release profile of MBGNPs determined by ICP-OES. The concentration of Si^{4+}, Ca^{2+}, Ce^{3+} and Ga^{3+} in PBS for 1, 3, 7 and 14 days.
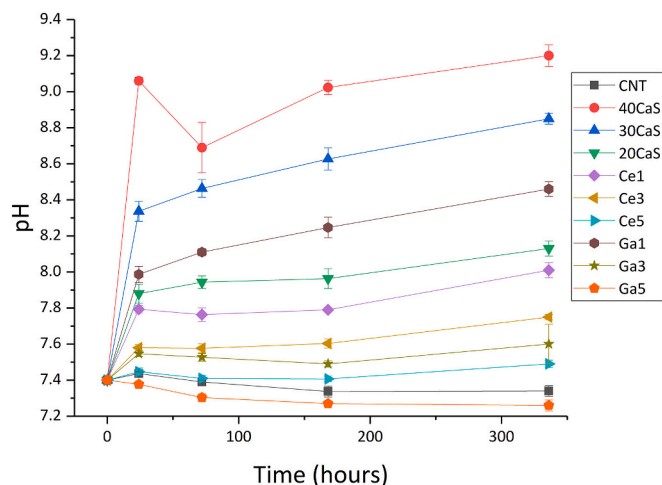

Fig. 10. – pH of PBS containing MBGNPs after 1, 3, 7 and 14 days of immersion.

the content of Ca being much lower (0.69% mol) than in other samples. Additionally, the concentrations of Ce leached to the solution were in all cases below the detection limit of the used analytical method. This observation is in line with the results of the leaching behavior of sol-gel based cerium-doped bioactive glasses prepared by other authors [18,31]. Ce ions can form insoluble complexes with phosphate groups [32], and therefore cannot be detected by ICP-OES.

For the Ga-doped MBGNPs, the concentrations of Si decreased with the increase of Ga content. This is attributed to an increased network connectivity due to lower Ca content in nanoparticles with a higher level of Ga doping. Ga has a stabilizing effect on the glass network. Gallium ions show intermediate behavior between network formers and modifiers, and act as network former, altering and increasing the network connectivity [53]. Similarly to Ce-doped nanoparticles, a burst release of Ca was observed after 1 day of immersion for the Ga1 composition. For Ga3 composition, after an initial fast increase, the content of Ca in the solution started to decline after 3 days of immersion. The highest concentration of Ca for the Ga5 composition was measured after 7 days of immersion. The release profiles of Ga corresponded to the compositions of the tested MBGNPs.

The pH change of the extracts of MBGNPs during the immersion test in PBS was recorded and is shown in Fig. 10. After immersion for 14 days, all samples except Ga5 (value of pH 7.26 ± 0.03), showed higher pH values compared to the blank (pH 7.34 ± 0.03). 40CaS composition showed the highest pH value (pH 9.20 ± 0.06) due to the high specific surface area and the amount of Ca^{2+} ions released. The release of Ca^{2+} ions is likely responsible for the pH values of the extracts, while the release of Ga^{3+} did not show any significant effect on the pH.

These findings cannot be directly translated to clinical applications (in vivo conditions) as the solutions were not changed at any point throughout the incubation. Therefore, the conditions do not account for the dynamic physiological conditions in the body. Also, it is known [54] that bioactive glasses do not exhibit the same dissolution behavior in cell or bacteria culture media. Additionally, the presence of amino acids and other organic molecules is known to setback the formation of the surface apatite layer on bioactive materials [55]. Nevertheless, understanding the dissolution behavior of MBGNPs and monitoring the ion release and pH changes are essential for their further biomedical applications.
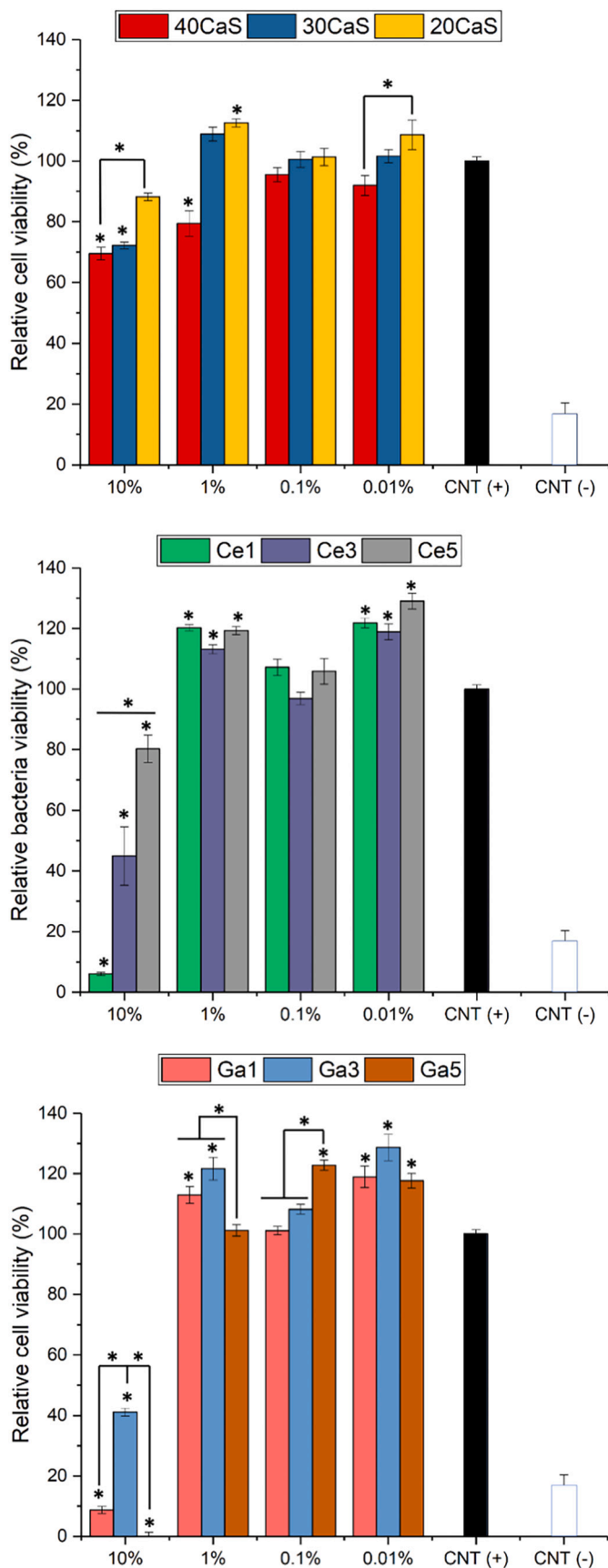
Fig. 11. Relative viability of MG-63 cells cultured with the extract of MBGNPs in 10, 1, 0.1 and 0.01% w/v cell culture medium dilutions ($n = 9$, CNT = control, samples in triplicate,* $p < 0.05$).

3.4. In-vitro biocompatibility

The MG-63 cell viability in the presence of extracts of MBGNPs is shown in Fig. 11. The absorbance of positive control, i.e. the cells cultured only with cell culture medium, was normalized as 100%. In general, after 48 h of culture, the cell viability increased with the higher dilution of the MBGNPs extracts. The cells cultured with 10% *w/v* extracts of Ce1, Ga1, and Ga5 compositions showed the lowest cell viability. For the xCaS series of MBGNPS, the cells cultured with the extracts of 20CaS showed significantly higher viability compared to that of 40CaS with 10% w/v extract. Moreover, 1% *w/v* extract of 20CaS sample showed significantly higher cell viability compared to the positive control within the xCaS series of MBGNPs. For Ce-doped MBGNPs, 1 and 0.01% w/v extracts showed significantly better cell viability than the positive control group, without significant differences for the various doping contents. The 10% w/v extract of the Ga doped MBGNPs decreased the cell viability. Ga^{3+} shares similarities with Fe^{3+} and it could bond with iron-binding proteins [56]. Therefore, gallium could disrupt protein functions and lead to negative downstream effects on cells [56]. Hence, in 10% w/v extract the high amount of Ga^{3+} ions could cause negative effects on cells. In diluted extracts, the cell viability significantly improved and led to markedly improved cell viability with 0.01% w/v extract compared to the positive control.

Optical microscopy images of H&E-stained MG-63 cells cultured with the 1% w/v extracts of MBGNPs, which do not affect cytocompatibility, as well as the positive and negative control, are shown in Fig. 12. The cells were oval to spindle-shaped, which is their typical cell morphology [57]. Furthermore, the cell confluence was correlated with cell viability measured by WST-8 assay.

3.5. Antibacterial activity of MBGNPs

The antibacterial activities of the MBGNPs were tested using *S. aureus* (Gram-positive) and *E. coli* (Gram-negative) bacteria. The concentration of 1% w/v MBGNPs extracts did not show cytotoxicity according to the in vitro biocompatibility study and therefore it was selected for the antibacterial test. Before the addition of bacteria to the extracts of the 1% *w/v* MBGNPs in LB medium, the pH was measured to study the effect of pH variation on antibacterial activity (Fig. 13). The measured value for LB medium was pH 7, which is optimal for the growth of bacteria. However, it increased up to pH 8.5 after the addition of MBGNPs after 1 day of incubation. pH changes reflect the amount of calcium content in the MBGNPs. Compositions like Ce5 and Ga5, which contain a low amount of Ca, did not show any increase in pH values. The viability of both bacteria strains is shown in Fig. 14. The absorbance of the control, with bacteria cultured only with LB medium, was normalized as 100%.

The xCaS series showed an inhibition effect on both bacteria strains. The highest inhibition effect was observed after 6 h of incubation for Gram-positive bacteria. After that, the inhibitory effect of the MBGNPs decreased. However, there were no significant differences between the different amounts of CaO. On the other hand, the 30CaS sample showed the highest inhibition effect for Gram-negative bacteria after 6 h of incubation, and all undoped MBGNPs maintained their inhibitory effect for Gram-negative bacteria even after 24 h. The inhibition effect of xCaS series MBGNPs was mainly because of the increased osmolarity, osmotic pressure, and the change of pH caused by ions release [58]. Bioactive glasses commonly increase the pH in solutions, but the pH also depends on the dissolution medium, particularly if a buffer solution is used as the medium [55]. The rising pH values create a hostile environment for bacteria, which leads to changes in their morphology [59,60]. Ce-doped MBGNPs showed lower viabilities of Gram-positive bacteria than the control group, and it was most effective after 6-h of incubation. The Ce3 sample showed a significantly higher inhibition effect than Ce1 and Ce5 compositions. Moreover, Ce1 was more effective against Gram-negative bacteria after 24-h incubation than Ce3 and Ce5 compositions. The Ga
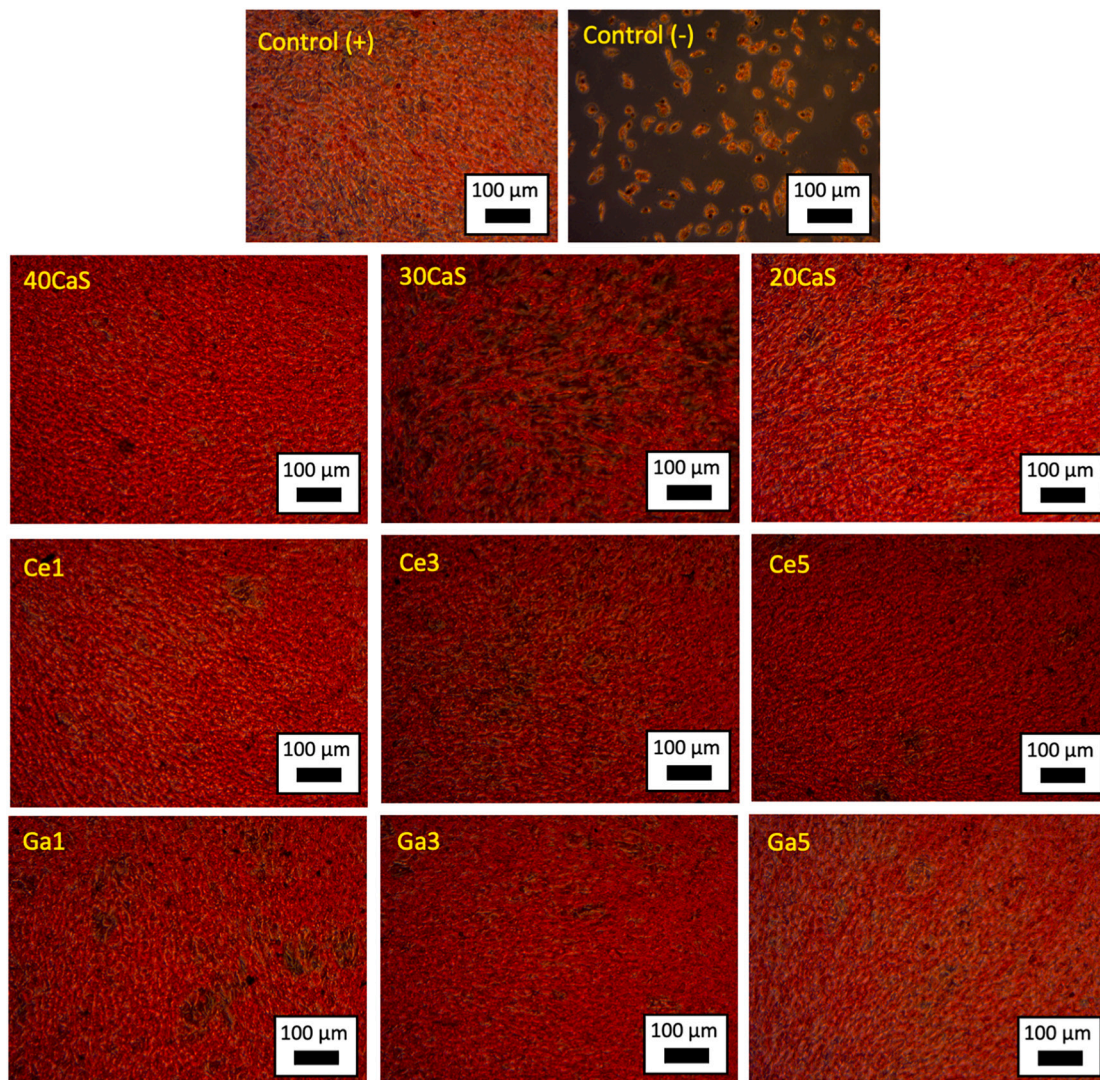
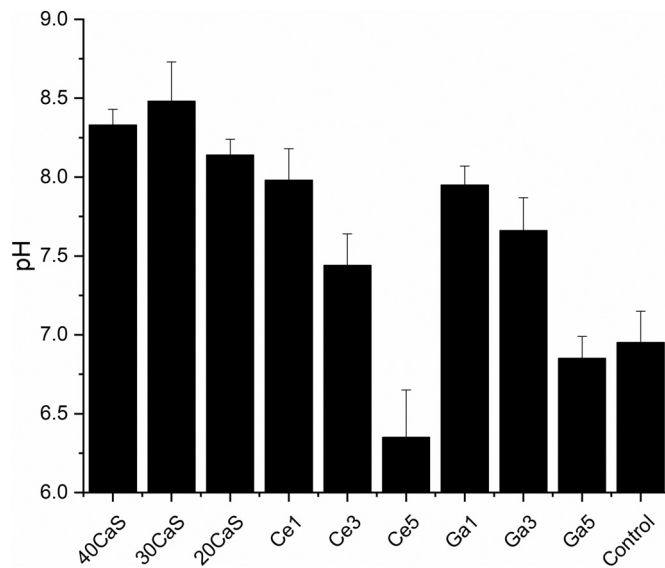**Fig. 12.** Optical microscopy images of H&E-stained MG-63 cells cultured with the 1% w/v extracts of MBGNPs.

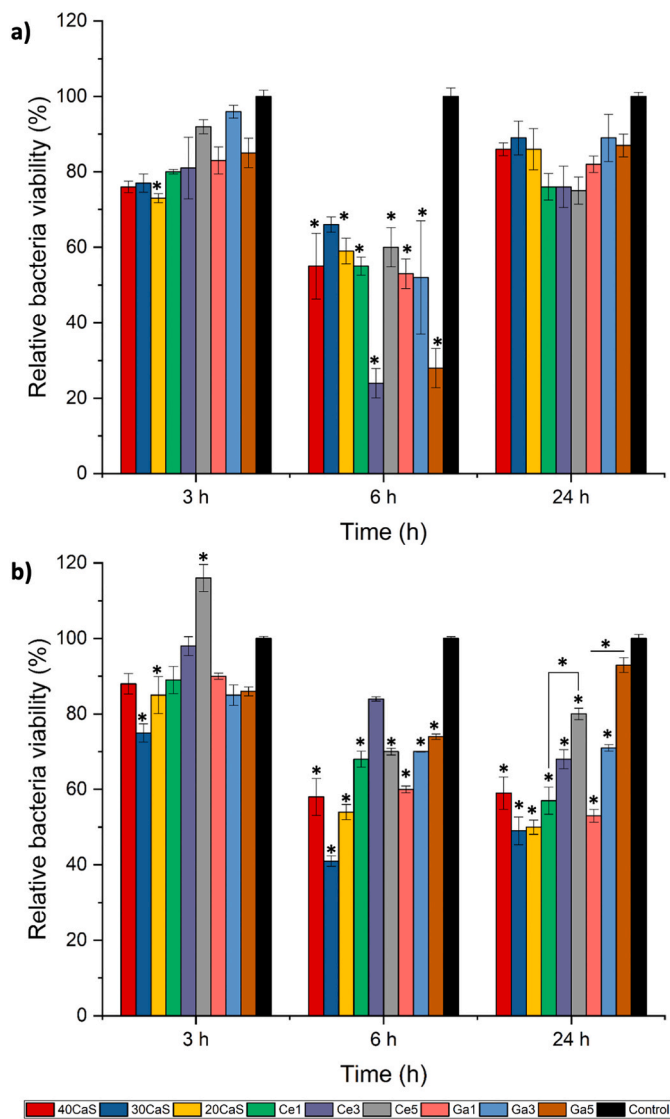**Fig. 13.** pH changes of 1% *w/v* MBGNPs in LB medium after 1d of incubation.

Fig. 14. Antibacterial activity of MBGNPs after 3, 6, and 24 h incubation with a) *S. aureus* (Gram-positive) and b) *E. coli* (Gram-negative) bacteria ($n = 3$, samples in triplicate,* $p < 0.05$).

doped MBGNPs showed lower viabilities of both Gram-positive and Gram-negative bacteria than the control group. Moreover, the Ga5 sample showed the highest inhibition effect on Gram-positive bacteria after 6-h incubation. Additionally, the Ga1 composition showed the highest inhibition effect on Gram-negative bacteria after 6 and 24-h incubation, and there was a significant difference for Ga1 composition at 24-h incubation compared to Ga3 and Ga5 MBGNPs for Gram-negative bacteria. The different results between Gram-positive and Gram-negative bacteria strains might be due to different bacterial characteristics and morphology, e.g. the presence of a thin layer of peptidoglycan on Gram-negative bacteria compared to layer free Gram-positive bacteria [61].

4. Conclusions

Microemulsion-assisted sol-gel technique was successfully employed for the development of Ce and Ga doped mesoporous bioactive glass nanoparticles. Well dispersed spheroidal and pineal-shaped particles were obtained. Ce and Ga doped MBGNPs were based on the binary system $60SiO_2$-$40CaO$. Metallic ion additions resulted in the creation of a disordered mesoporous structure. XRD analysis confirmed that all

samples were amorphous except Ce5, which contained also CeO_2 nanoparticles with cubic crystal structure. BET results proved that MBGNPs were mesoporous, with high specific surface areas. All MBGNPs were bioactive. ICP-OES results indicated a relatively slow release of Ga ions. MBGNPs exhibited antibacterial properties against *S. aureus* and *E. coli*. Additionally, MBGNPs extracts did not exhibit any cytotoxicity towards MG-63 osteoblast-like cells. On the contrary, cell viability increased significantly with Ga and Ce doped MBGNPs except for the 10% w/v dilution extract. The novel Ce and Ga doped MBGNPs are candidates for multifunctional drug delivery vehicles and for bioactive fillers in biomedical applications. Future work will be focused on more detailed studies of possible cytotoxic and antibacterial effects in direct contact with MBGNPs, and on the development of various drug loading strategies.

CRediT author statement

Fatih Kurtuldu: Conceptualization, Validation, Investigation, Data curation, Writing – Original Draft, Visualization. **Nurshen Mutlu:** Validation, Investigation, Data curation, Writing – Review & Editing. **Martin Michálek:** Resources, Writing – Review & Editing. **Kai Zheng:** Methodology, Writing – Review & Editing. **Milan Masar:** Validation, Investigation, Data curation. **Liliana Liverani:** Validation, Writing – Review & Editing. **Si Chen:** Investigation, Writing – Review & Editing. **Dušan Galusek:** Conceptualization, Writing – Review & Editing, Supervision, Project administration, Funding acquisition. **Aldo R. Boccaccini:** Conceptualization, Writing – Review & Editing, Supervision, Project administration, Funding acquisition.

Declaration of competing interest

The authors declare that they have no known competing financial interests or personal relationships that could have appeared to influence the work reported in this paper.

Acknowledgments

References

[1] L.L. Hench, The story of bioglass®, J. Mater. Sci. Mater. Med. (2006) 967–978, https://doi.org/10.1007/s10856-006-0432-z.
[2] L.L. Hench, I. Thompson, Twenty-first century challenges for biomaterials, J. R. Soc. Interface 7 (2010) S379–S391, https://doi.org/10.1098/rsif.2010.0151.focus.
[3] V. Miguez-Pacheco, L.L. Hench, A.R. Boccaccini, Bioactive glasses beyond bone and teeth: emerging applications in contact with soft tissues, Acta Biomater. 13 (2015) 1–15, https://doi.org/10.1016/j.actbio.2014.11.004.
[4] L.L. Hench, Bioglass: 10 milestones from concept to commerce, J. Non-Cryst. Solids 432 (2016) 2–8, https://doi.org/10.1016/j.jnoncrysol.2014.12.038.
[5] L.L. Hench, J.R. Jones, Bioactive glasses: Frontiers and challenges, front, Bioeng. Biotechnol. 3 (2015) 1–12, https://doi.org/10.3389/fbioe.2015.00194.
[6] J.S. Beck, J.C. Vartuli, W.J. Roth, M.E. Leonowicz, C.T. Kresge, K.D. Schmitt, C.T. W. Chu, D.H. Olson, E.W. Sheppard, S.B. McCullen, J.B. Higgins, J.L. Schlenker, A new family of mesoporous molecular sieves prepared with liquid crystal templates, J. Am. Chem. Soc. 114 (1992) 10834–10843, https://doi.org/10.1021/ja00053a020.
[7] M. Vallet-Regi, A. Rámila, R.P. Del Real, J. Pérez-Pariente, A new property of MCM-41: drug delivery system, Chem. Mater. 13 (2001) 308–311, https://doi.org/10.1021/cm0011559.
[8] M. Vallet-Regí, Ordered mesoporous materials in the context of drug delivery systems and bone tissue engineering, Chem. - A Eur. J. 12 (2006) 5934–5943, https://doi.org/10.1002/chem.200600226.

[9] D. Arcos, A. López-Noriega, E. Ruiz-Hernández, O. Terasaki, M. Vallet-Regí, Ordered mesoporous microspheres for bone grafting and drug delivery, Chem. Mater. 21 (2009) 1000–1009, https://doi.org/10.1021/cm801649z.

[10] U. Ciesla, F. Schüth, Ordered mesoporous materials, Microporous Mesoporous Mater. 27 (1999) 131–149, https://doi.org/10.1016/S1387-1811(98)00249-2.

[11] I.I. Slowing, B.G. Trewyn, V.S.Y. Lin, Mesoporous silica nanoparticles for intracellular delivery of membrane-impermeable proteins, J. Am. Chem. Soc. 129 (2007) 8845–8849, https://doi.org/10.1021/ja0719780.

[12] S. Montalvo-Quiros, G. Aragoneses-Cazorla, L. Garcia-Alcalde, M. Vallet-Regí, B. González, J.L. Luque-Garcia, Cancer cell targeting and therapeutic delivery of silver nanoparticles by mesoporous silica nanocarriers: insights into the action mechanisms using quantitative proteomics, Nanoscale. 11 (2019) 4531–4545, https://doi.org/10.1039/c8nr07667g.

[13] M. Manzano, M. Vallet-Regí, Mesoporous silica nanoparticles for drug delivery, Adv, Funct. Mater. 30 (2019) 3–5, https://doi.org/10.1002/adfm.201902634.

[14] J.R. Jones, Reprint of: review of bioactive glass: from Hench to hybrids, Acta Biomater. 23 (2015) S53–S82, https://doi.org/10.1016/j.actbio.2015.07.019.

[15] K. Zheng, A.R. Boccaccini, Sol-gel processing of bioactive glass nanoparticles: a review, Adv, Colloid Interface Sci. 249 (2017) 363–373, https://doi.org/10.1016/j.cis.2017.03.008.

[16] Q. Liang, Q. Hu, G. Miao, B. Yuan, X. Chen, A facile synthesis of novel mesoporous bioactive glass nanoparticles with various morphologies and tunable mesostructure by sacrificial liquid template method, Mater. Lett. 148 (2015) 45–49, https://doi.org/10.1016/j.matlet.2015.01.122.

[17] Z. Neščáková, K. Zheng, L. Liverani, Q. Nawaz, D. Galusková, H. Kaňková, M. Michálek, D. Galusek, A.R. Boccaccini, Multifunctional zinc ion doped sol – gel derived mesoporous bioactive glass nanoparticles for biomedical applications, Bioact. Mater. 4 (2019) 312–321, https://doi.org/10.1016/j.bioactmat.2019.10.002.

[18] K. Zheng, E. Torre, A. Bari, N. Taccardi, C. Cassinelli, M. Morra, S. Fiorilli, C. Vitale-Brovarone, G. Iviglia, A.R. Boccaccini, Antioxidant mesoporous Ce-doped bioactive glass nanoparticles with anti-inflammatory and pro-osteogenic activities, Mater. Today Bio. 5 (2020), 100041, https://doi.org/10.1016/j.mtbio.2020.100041.

[19] I. Izquierdo-Barba, A.J. Salinas, M. Vallet-Regí, Bioactive glasses: from macro to Nano, Int. J. Appl. Glas. Sci. 4 (2013) 149–161, https://doi.org/10.1111/ijag.12028.

[20] C. Vichery, J.M. Nedelec, Bioactive glass nanoparticles: from synthesis to materials design for biomedical applications, Materials (Basel). 9 (2016), https://doi.org/10.3390/ma9040288.

[21] S. Schacht, Q. Huo, I.G. Voigt-Martin, G.D. Stucky, F. Schuth, Oil-water Interface templating of mesoporous macroscale structures, Science (80-.). 273 (1996) 768–771. doi:https://doi.org/10.1126/science.273.5276.768.

[22] Q. Nawaz, M.A.U. Rehman, A. Burkovski, J. Schmidt, A.M. Beltrán, A. Shahid, N. K. Alber, W. Peukert, A.R. Boccaccini, Synthesis and characterization of manganese containing mesoporous bioactive glass nanoparticles for biomedical applications, J. Mater. Sci. Mater. Med. 29 (2018) 64, https://doi.org/10.1007/s10856-018-6070-4.

[23] K. Zheng, P. Balasubramanian, T. Paterson, R. Stein, S. MacNeil, S. Fiorilli, C. Vitale-Brovarone, J. Shepherd, A.R. Boccaccini, Ag modified mesoporous bioactive glass nanoparticles for enhanced antibacterial activity in 3D infected skin model, Mater. Sci. Eng. C 103 (2019) 109764. doi:https://doi.org/10.1016/j.msec.2019.109764.

[24] M. Vallet-Regí, M. Colilla, I. Izquierdo-Barba, M. Manzano, Mesoporous silica nanoparticles for drug delivery: current insights, Molecules. 23 (2017) 47, https://doi.org/10.3390/molecules23010047.

[25] S. Chen, S.L. Greasley, Z.Y. Ong, P. Naruphontjirakul, S.J. Page, J.V. Hanna, A. N. Redpath, O. Tsigkou, S. Rankin, M.P. Ryan, A.E. Porter, J.R. Jones, Biodegradable zinc-containing mesoporous silica nanoparticles for cancer therapy, Mater. Today Adv. 6 (2020), 100066, https://doi.org/10.1016/j.mtadv.2020.100066.

[26] M. Gisbert-Garzarán, M. Manzano, M. Vallet-Regí, Mesoporous silica nanoparticles for the treatment of complex bone diseases: bone cancer, bone infection and osteoporosis, Pharmaceutics. 12 (2020), https://doi.org/10.3390/pharmaceutics12010083.

[27] S. Kaya, M. Cresswell, A.R. Boccaccini, Mesoporous silica-based bioactive glasses for antibiotic-free antibacterial applications, Mater. Sci. Eng. C 83 (2018) 99–107, https://doi.org/10.1016/j.msec.2017.11.003.

[28] T.E. Paterson, A. Bari, A.J. Bullock, R. Turner, G. Montalbano, S. Fiorilli, C. Vitale-Brovarone, S. MacNeil, J. Shepherd, Multifunctional copper-containing mesoporous glass nanoparticles as antibacterial and proangiogenic agents for chronic wounds, front, Bioeng. Biotechnol. 8 (2020) 1–14, https://doi.org/10.3389/fbioe.2020.00246.

[29] I. Atkinson, E.M. Anghel, S. Petrescu, A.M. Seciu, L.M. Stefan, O.C. Mocioiu, L. Predoana, M. Voicescu, S. Somacescu, D. Culita, M. Zaharescu, Cerium-containing mesoporous bioactive glasses: Material characterization, in: Vitro Bioactivity, Biocompatibility and Cytotoxicity Evaluation, Microporous Mesoporous Mater 276, 2019, pp. 76–88, https://doi.org/10.1016/j.micromeso.2018.09.029.

[30] G. Zhou, G. Gu, Y. Li, Q. Zhang, W. Wang, S. Wang, J. Zhang, Effects of cerium oxide nanoparticles on the proliferation, differentiation, and mineralization function of primary osteoblasts in vitro, biol, Trace Elem. Res. 153 (2013) 411–418, https://doi.org/10.1007/s12011-013-9655-2.

[31] S. Shruti, A.J. Salinas, G. Malavasi, G. Lusvardi, L. Menabue, C. Ferrara, P. Mustarelli, M. Vallet-Regì, Structural and in vitro study of cerium, gallium and

[32] A.J. Salinas, S. Shruti, G. Malavasi, L. Menabue, M. Vallet-Regí, Substitutions of cerium, gallium and zinc in ordered mesoporous bioactive glasses, Acta Biomater. 7 (2011) 3452–3458, https://doi.org/10.1016/j.actbio.2011.05.033.

[33] V. Nicolini, G. Malavasi, L. Menabue, G. Lusvardi, F. Benedetti, S. Valeri, P. Luches, Cerium-doped bioactive 45S5 glasses: spectroscopic, redox, bioactivity and biocatalytic properties, J. Mater. Sci. 52 (2017) 8845–8857, https://doi.org/10.1007/s10853-017-0867-2.

[34] E. Varini, S. Sánchez-Salcedo, G. Malavasi, G. Lusvardi, M. Vallet-Regí, A.J. Salinas, Cerium (III) and (IV) containing mesoporous glasses/alginate beads for bone regeneration: bioactivity, biocompatibility and reactive oxygen species activity, Mater. Sci. Eng. C 105 (2019) 109971. doi:https://doi.org/10.1016/j.msec.2019.109971.

[35] C.R. Chitambar, The therapeutic potential of iron-targeting gallium compounds in human disease: from basic research to clinical application, Pharmacol. Res. 115 (2017) 56–64, https://doi.org/10.1016/j.phrs.2016.11.009.

[36] S. Pourshahrestani, E. Zeimaran, N.A. Kadri, N. Gargiulo, S. Samuel, S.V. Naveen, T. Kamarul, M.R. Towler, Gallium-containing mesoporous bioactive glass with potent hemostatic activity and antibacterial efficacy, J. Mater. Chem. B 4 (2016) 71–86, https://doi.org/10.1039/c5tb02062j.

[37] S. Shruti, A.J. Salinas, G. Lusvardi, G. Malavasi, L. Menabue, M. Vallet-Regi, Mesoporous bioactive scaffolds prepared with cerium-, gallium- and zinc-containing glasses, Acta Biomater. 9 (2013) 4836–4844, https://doi.org/10.1016/j.actbio.2012.09.024.

[38] A.L.B. Maçon, T.B. Kim, E.M. Valliant, K. Goetschius, R.K. Brow, D.E. Day, A. Hoppe, A.R. Boccaccini, I.Y. on. Kim, C. Ohtsuki, T. Kokubo, A. Osaka, M. Vallet-Regí, D. Arcos, L. Fraile, A.J. Salinas, A. V. Teixeira, Y. Vueva, R.M. Almeida, M. Miola, C. Vitale-Brovarone, E. Verné, W. Höland, J.R. Jones, A unified in vitro evaluation for apatite-forming ability of bioactive glasses and their variants, J. Mater. Sci. Mater. Med. 26 (2015) 115. doi:https://doi.org/10.1007/s10856-015-5403-9.

[39] T. Kokubo, H. Takadama, How useful is SBF in predicting in vivo bone bioactivity? Biomaterials. 27 (2006) 2907–2915, https://doi.org/10.1016/j.biomaterials.2006.01.017.

[40] K. Shiba, S. Motozuka, T. Yamaguchi, N. Ogawa, Y. Otsuka, K. Ohnuma, T. Kataoka, M. Tagaya, Effect of cationic surfactant micelles on hydroxyapatite nanocrystal formation: an investigation into the inorganic-organic interfacial interactions, Cryst, Growth Des. 16 (2016) 1463–1471, https://doi.org/10.1021/acs.cgd.5b01599.

[41] Z.A. Alothman, A review: fundamental aspects of silicate mesoporous materials, Materials (Basel). 5 (2012) 2874–2902, https://doi.org/10.3390/ma5122874.

[42] K. Zheng, J. Kang, B. Rutkowski, M. Gawęda, J. Zhang, Y. Wang, N. Founier, M. Sitarz, N. Taccardi, A.R. Boccaccini, Toward highly dispersed mesoporous bioactive glass nanoparticles with high cu concentration using cu/ascorbic acid complex as precursor, Front. Chem. 7 (2019) 1–15, https://doi.org/10.3389/fchem.2019.00497.

[43] N. Thakur, P. Manna, J. Das, Synthesis and biomedical applications of nanoceria, a redox active nanoparticle, J. Nanobiotechnology. 17 (2019) 1–27, https://doi.org/10.1186/s12951-019-0516-9.

[44] S. Kumar, M. Srivastava, J. Singh, S. Layek, M. Yashpal, A. Materny, A.K. Ojha, Controlled synthesis and magnetic properties of monodispersed ceria nanoparticles, AIP Adv. 5 (2015), https://doi.org/10.1063/1.4908003.

[45] M.T. Matter, L.A. Furer, F.H.L. Starsich, G. Fortunato, S.E. Pratsinis, I.K. Herrmann, Engineering the bioactivity of flame-made ceria and ceria/bioglass hybrid nanoparticles, ACS Appl. Mater. Interfaces 11 (2019) 2830–2839, https://doi.org/10.1021/acsami.8b18778.

[46] M.M. Ali, H.S. Mahdi, A. Parveen, A. Azam, Optical properties of cerium oxide (CeO2) nanoparticles synthesized by hydroxide mediated method, AIP Conf. Proc. 1953 (2018) 1–5, https://doi.org/10.1063/1.5032379.

[47] R. Verma, S.K. Samdarshi, S. Bojja, S. Paul, B. Choudhury, A novel thermophotocatalyst of mixed-phase cerium oxide (CeO2/Ce2O3) homocomposite nanostructure: role of interface and oxygen vacancies, Sol. Energy Mater. Sol. Cells 141 (2015) 414–422, https://doi.org/10.1016/j.solmat.2015.06.027.

[48] H. Aguiar, P. González, J. Serra, Bioactive glass structure and solubility, in: Bioact. Glas., Second Ed, Elsevier, 2018, pp. 37–61, https://doi.org/10.1016/B978-0-08-100936-9.00002-2.

[49] J.K. Christie, R.I. Ainsworth, N.H. De Leeuw, Investigating structural features which control the dissolution of bioactive phosphate glasses: beyond the network connectivity, J. Non-Cryst. Solids 432 (2016) 31–34, https://doi.org/10.1016/j.jnoncrysol.2015.01.016.

[50] R.P. Senthilkumar, V. Bhuvaneshwari, R. Ranjithkumar, S. Sathiyavimal, V. Malayaman, B. Chandarshekar, Synthesis, characterization and antibacterial activity of hybrid chitosan-cerium oxide nanoparticles: as a bionanomaterials, Int. J. Biol. Macromol. 104 (2017) 1746–1752, https://doi.org/10.1016/j.ijbiomac.2017.03.139.

[51] A. Martinez, I. Izquierdo-Barba, M. Vallet-Regi, Bioactivity of a CaO - SiO2 binary glasses system, Chem. Mater. 12 (2000) 3080–3088, https://doi.org/10.1021/cm001107o.

[52] H. Liu, H. Yazici, C. Ergun, T.J. Webster, H. Bermek, An in vitro evaluation of the ca/P ratio for the cytocompatibility of nano-to-micron particulate calcium phosphates for bone regeneration, Acta Biomater. 4 (2008) 1472–1479, https://doi.org/10.1016/j.actbio.2008.02.025.

[53] S. Sanchez-Salcedo, G. Malavasi, A.J. Salinas, G. Lusvardi, L. Rigamonti, L. Menabue, M. Vallet-Regi, Highly-bioreactive silica-based mesoporous bioactive

glasses enriched with gallium(III), Materials (Basel). 11 (2018) 1–17, https://doi.org/10.3390/ma11030367.

[54] A. Nommeots-Nomm, L. Hupa, D. Rohanová, D.S. Brauer, A review of acellular immersion tests on bioactive glasses—influence of medium on ion release and apatite formation, Int. J. Appl. Glas. Sci. 11 (2020) 537–551, https://doi.org/10.1111/ijag.15006.

[55] F.A. Shah, D.S. Brauer, R.M. Wilson, R.G. Hill, K.A. Hing, Influence of cell culture medium composition on in vitro dissolution behavior of a fluoride-containing bioactive glass, J. Biomed. Mater. Res. - Part A. 102 (2014) 647–654, https://doi.org/10.1002/jbm.a.34724.

[56] C.R. Chitambar, W.E. Antholine, Iron-targeting antitumor activity of gallium compounds and novel insights into triapine®-metal complexes, Antioxid. Redox Signal. 18 (2013) 956–972, https://doi.org/10.1089/ars.2012.4880.

[57] S. Staehlke, H. Rebl, B. Nebe, Phenotypic stability of the human MG-63 osteoblastic cell line at different passages, Cell Biol. Int. 43 (2019) 22–32, https://doi.org/10.1002/cbin.11073.

[58] S. Ray, S. Dasgupta, First principle study on in-vitro antimicrobial properties of nano 52S4.6 bioactive glass, Ceram. Int. (2020) 0–1, https://doi.org/10.1016/j.ceramint.2020.02.182.

[59] K. Schuhladen, L. Stich, J. Schmidt, A. Steinkasserer, A.R. Boccaccini, E. Zinser, Cu, Zn doped borate bioactive glasses: antibacterial efficacy and dose-dependent: in vitro modulation of murine dendritic cells, Biomater. Sci. 8 (2020) 2143–2155, https://doi.org/10.1039/c9bm01691k.

[60] E. Munukka, O. Leppäranta, M. Korkeamäki, M. Vaahtio, T. Peltola, D. Zhang, L. Hupa, H. Ylänen, J.I. Salonen, M.K. Viljanen, E. Eerola, Bactericidal effects of bioactive glasses on clinically important aerobic bacteria, J. Mater. Sci. Mater. Med. 19 (2008) 27–32, https://doi.org/10.1007/s10856-007-3143-1.

[61] S. Kargozar, M. Montazerian, S. Hamzehlou, H.W. Kim, F. Baino, Mesoporous bioactive glasses: promising platforms for antibacterial strategies, Acta Biomater. 81 (2018) 1–19, https://doi.org/10.1016/j.actbio.2018.09.052.